

## Collision detection of convex polyhedra on the NVIDIA GPU architecture for the discrete element method



Nicolin Govender<sup>a,b,\*</sup>, Daniel N. Wilke<sup>b</sup>, Schalk Kok<sup>b</sup>

<sup>a</sup>Advanced Mathematical Modeling CSIR, Pretoria 0001, South Africa

<sup>b</sup>University of Pretoria, Department of Mechanical and Aeronautical Engineering, Pretoria 0001, South Africa

### ARTICLE INFO

**Keywords:**

GPU  
DEM  
Polyhedra  
CUDA  
Collision detection  
NVIDIA

### ABSTRACT

Convex polyhedra represent granular media well. This geometric representation may be critical in obtaining realistic simulations of many industrial processes using the discrete element method (DEM). However detecting collisions between the polyhedra and surfaces that make up the environment and the polyhedra themselves is computationally expensive. This paper demonstrates the significant computational benefits that the graphical processor unit (GPU) offers DEM. As we show, this requires careful consideration due to the architectural differences between CPU and GPU platforms. This paper describes the DEM algorithms and heuristics that are optimized for the parallel NVIDIA Kepler GPU architecture in detail. This includes a GPU optimized collision detection algorithm for convex polyhedra based on the separating plane (SP) method. In addition, we present heuristics optimized for the parallel NVIDIA Kepler GPU architecture. Our algorithms have minimalistic memory requirements, which enables us to store data in the limited but high bandwidth constant memory on the GPU. We systematically verify the DEM implementation, where after we demonstrate the computational scaling on two large-scale simulations. We are able achieve a new performance level in DEM by simulating 34 million polyhedra on a single NVIDIA K6000 GPU. We show that by using the GPU with algorithms tailored for the architecture, large scale industrial simulations are possible on a single graphics card.

© 2014 Elsevier Inc. All rights reserved.

### 1. Introduction

The discrete element method (DEM) approach which was first described by Cundall and Strack [1], is one of the most successful methods to simulate granular media (GM) [2–5]. DEM simulations require that all particles in the system have to be checked for contact at each time step, which involves a considerable number of calculations depending on particle geometry and number of particles [6]. To reduce the computational cost, particle shape is often approximated by spheres, for which contact detection is trivial. This approximation however results in the system exhibiting unrealistic mechanical behavior, as discussed by Latham and Munjiza [7,8]. Polyhedral shaped particles represent most GM well and hence exhibit realistic mechanical behavior to that of the actual system [9,10]. However, the number of polyhedral particles that can be simulated on typical workstation computers in a realistic time frame is limited, as discussed by Mack [11], in which only 322 polyhedra are simulated. This limitation is due primarily to complex collision detection and storage costs of the polyhedra.

\* Corresponding author at: Advanced Mathematical Modeling CSIR, Pretoria 0001, South Africa.

Driven by the demand for real-time 3D graphics, with prices kept low due to high selling volumes from the consumer gaming market, the programmable Graphic Processor Unit (GPU) offers cluster type performance at a fraction of the cost [12]. The parallel nature of the GPU allows a large number of simple independent processes to be executed in parallel. This results in significant speed ups over CPU implementations, for suitable algorithms.

## 2. The graphical processor unit (GPU)

**Fig. 1** shows the hardware design of the CPU and GPU processor chips. We see a major difference in the number of cores and threads present on each chip. CPU cores are designed to be general purpose, hence they are able to do complex logical operations such as running an operating system while being able to perform arithmetical operations. The closest equivalent of a CPU core on a GPU is a Streaming Multi-Processor (SM) which has most of its transistors as dedicated Arithmetic Logic Units (ALU), rather than control and cache, as in the case of the CPU [13]. GPUs are designed to render graphics, which involves the simultaneous manipulation of millions of pixels. This requires many parallel algebraic operations, hence the large amount of ALUs. Thus applications which require a large number of parallel arithmetic operations see a performance benefit on the GPU. The GPU has two memory spaces: on-chip memory (shared and constant memory) which is very fast but limited in size and scope; and off-chip memory (global-memory) which is much more plentiful and can be accessed by all SMs as well as the CPU. Global-memory is however about one hundred times slower than on-chip memory and can cause major performance degradation if not used efficiently and correctly.

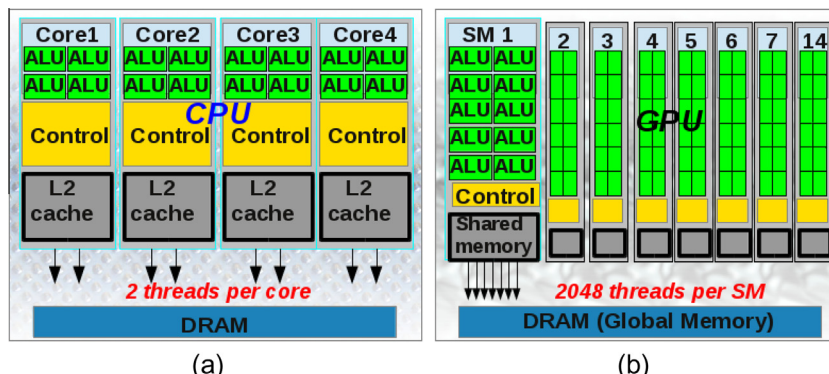
**Fig. 2** illustrates typical tasks at which each unit excels, in terms of computational performance. GPUs beat the flexible CPUs in spite of their considerably lower clock rate when processing similar data packets. Each CPU core is capable of launching two threads which can work independently and perform complex logical operations. Each SM on a Kepler GK110 GPU can launch 2048 threads which are only capable of performing the same task (Single Instruction Multiple Data (SIMD)) [14]. The NVIDIA Kepler architecture has a lower clock speed than the previous generation Fermi architecture but has more SMs, which benefits applications that have thread level parallelism such as DEM, provided we make certain assumptions to decouple the problem [15,16].

In this paper we exploit the computational power of the GPU via the NVIDIA developed CUDA programming model [14], which allows us to issue commands to the GPU from C++ code as opposed to a graphics language like OpenGL. CUDA allows us to create thousands of thread blocks containing millions of threads which get scheduled for execution on the hardware as SMs become available (we do not have control over the execution order of the blocks). The execution of a block only completes once all the threads within the block have reached an end point. This is very important and requires us to design algorithms that require similar times to complete for all threads to best utilize the parallelism on the GPU.

## 3. Polyhedra contact detection

Contact detection in DEM usually consists of two phases. The first phase, referred to as the broad phase, is computationally cheap and aims to reduce the number of contact pairs to only the nearest neighbors, as only they can be in possible physical contact. A review of various broad phase algorithms is given by Jimenez and Segura [17]. We use a highly efficient hashed grid approach that executes in parallel on the GPU, that is part of the code BLAZE-DEM developed by the authors [16]. In the second phase, referred to as the narrow phase, pairs of contacting particles obtained from the first phase are considered in detail to determine if they are indeed in contact. Depending on the contact resolution algorithm either contact points [9], or a contact volume [18] can be computed to determine the contact forces.

Several approaches for narrow phase polyhedral collision detection can be found in literature [9,18,19]. However, these algorithms require either complex geometrical or algebraic operations with some requiring iterative procedures, as discussed by Nassauer and Liedke [18]. In order to achieve performance gains on the GPU we must formulate an algorithm that is well suited to the light-weight threading model of the GPU (Section 2) with minimal storage requirements.



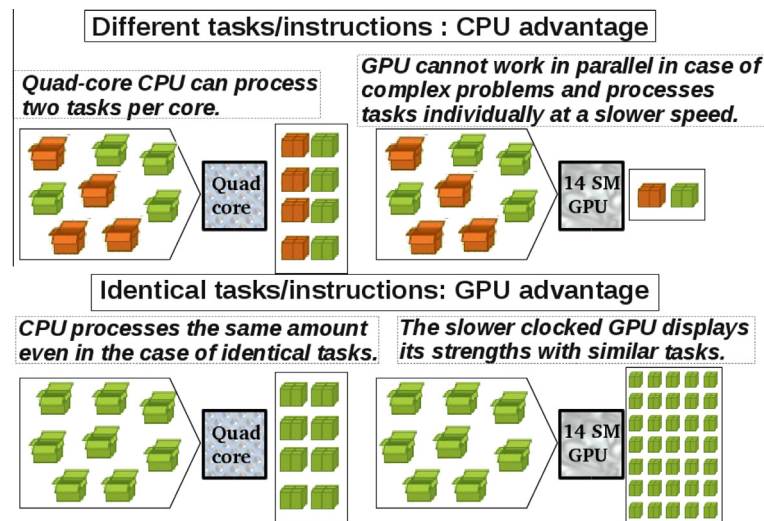


Fig. 2. Comparison between an i7 Quad-core CPU and NVIDIA GK110 GPU task processing.

### 3.1. Particle representation

By restricting our analysis to only convex particles we can represent a polyhedron as a collection of half-spaces  $f_i(\mathbf{n}, \mathbf{c})$ , as illustrated in Fig. 3. The half-space subtended by a face of a convex polyhedron partitions  $\mathbb{R}^3$  space into two distinct regions. The first region  $f_i(\mathbf{n}, \mathbf{c}) \leq 0$  contains the entire polyhedron, while the second region  $f_i(\mathbf{n}, \mathbf{c}) > 0$  is an infinite half-space in the direction indicated by the normal to the face [20].

The choice of faces to define a polyhedron means that we only need to store the vertices  $\mathbf{v}_i$ ,  $i = 1, \dots, n$ , face normals  $\mathbf{n}_j$ ,  $j = 1, \dots, m$  and face centroids  $\mathbf{c}_j$ ,  $j = 1, \dots, m$ . This minimalistic representation allows us to place data structures in the faster limited constant memory (48 KB) on the GPU, as depicted in Fig. 4. We hard code the maximum number of features to 32 due to the small size of constant memory.

### 3.2. World representation

A common approach in DEM simulations is to model the surfaces of the environment as actual particles [21]. This increases computational storage requirements and reduces the task level parallelism that can be exploited on the GPU. We adopt a similar approach as used in the gaming industry [16], in that we model the environment as separate geometric objects (world). World geometry is modeled as either a collection of planar quadrilaterals of the form  $S(\mathbf{n}, \mathbf{c})$ , where  $\mathbf{n}$  is the

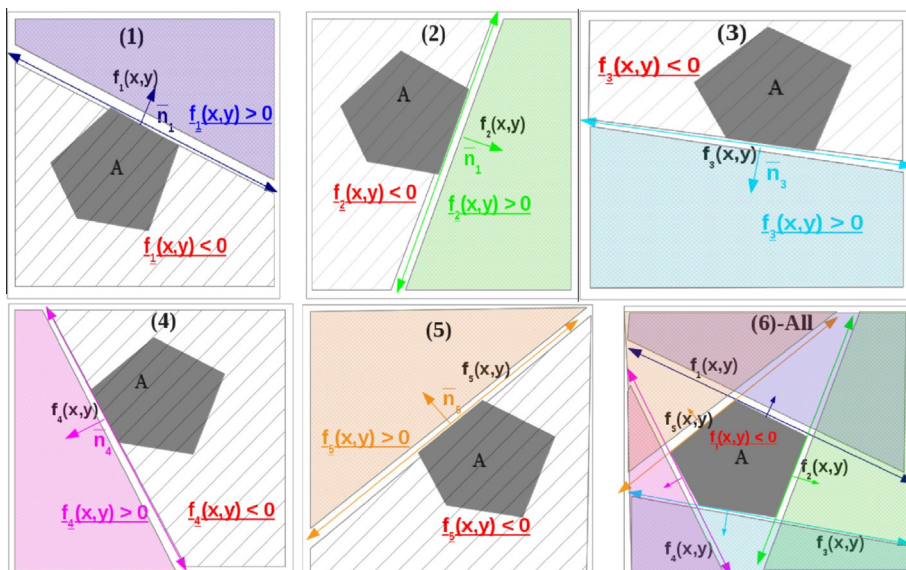
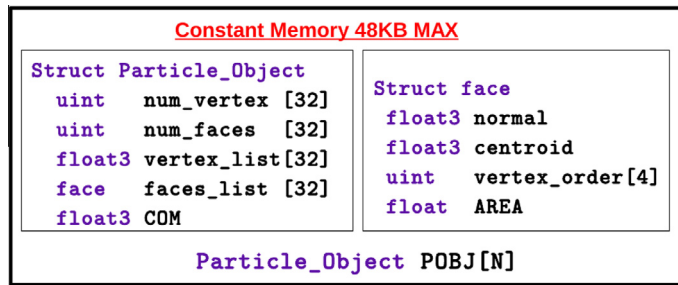


Fig. 3. Planar polygon representation.

**Fig. 4.** Particle object representation.

normal and **c** the centroid of the surface, or geometric objects that have a closed form expression such as a cylinder which we denote as “macro objects”. A world can consist of a single object, as illustrated in Fig. 5(a), or a combination of objects, as illustrated Fig. 5(b), which shows a drum (labeled 1) and blades (labeled 2 and 3).

We make a further distinction in that we split world objects in two classes:

1. Internal: all surface normals point inwards (Fig. 5(a) and label 1 in Fig. 5(b)).
2. External: surface normals can have any orientation (labels 2 and 3 in Fig. 5(b)).

This distinction allows us to reduce the computational cost of collision detection between a polyhedron and the world object. Consider Fig. 6, which shows the different types of contact between polyhedra. Type 1 is the quickest to solve and the most frequent, while Type 2 is more complex but far less frequent in typical GM simulations (see for example Fig. 33). For an internal object it is only necessary to check for Type 1 contact (vertex–face or face–face), as it is impossible to have edge–edge contact. Therefore we decompose non-convex boundaries into multiple convex boundaries where possible as shown in Fig. 5(b), in which we model the blades as external objects and the drum as a cylinder, which is an internal object.

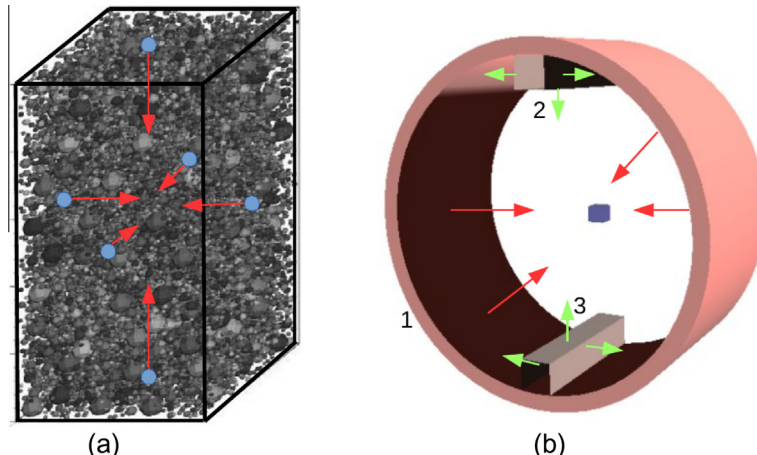
### 3.3. Theoretical formulation

The three scenarios depicted in Fig. 7, represent all possible geometric configurations of a polyhedron  $\mathcal{A}$  and a planar surface  $P$ . We represent the planar surface  $P$  by the half-space  $S(\mathbf{n}, \mathbf{c}) > 0$ . The distance between a vertex  $\mathbf{v}$  and the planar surface  $P$  is given by:

$$d = \mathbf{n} \cdot (\mathbf{v} - \mathbf{c}) \quad (1)$$

where:

- $d > 0$  implies that the point is within the half-space  $S(\mathbf{n}, \mathbf{c}) < 0$ .
- $d = 0$  implies that the point is on the hyperplane boundary of the half-space.
- $d < 0$  implies that the point is penetrating the half-space  $S(\mathbf{n}, \mathbf{c}) > 0$ .

**Fig. 5.** World Object Types.

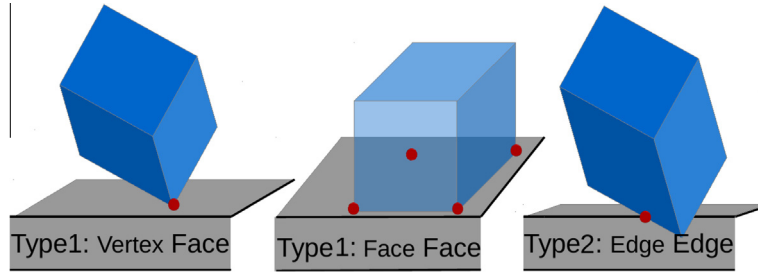


Fig. 6. Polyhedra surface contact types.

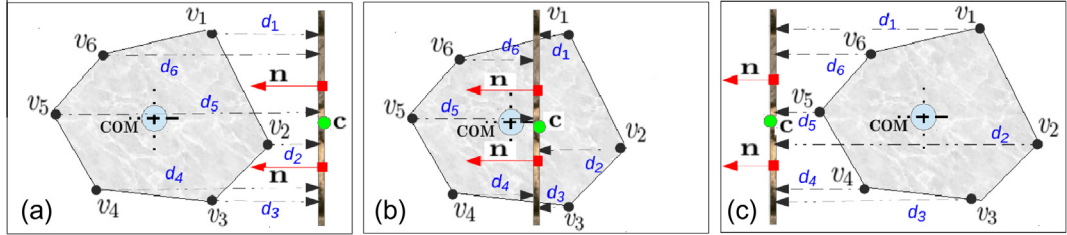


Fig. 7. Illustration of Theorem 1 in 2D.

**Fig. 7(a)** represents a scenario where there is clearly no penetration between  $\mathcal{A}$  and  $S$ . For this case, we have  $d_i > 0$  for  $i = 1, 2, \dots, 6$ . **Fig. 7(b)** depicts part of  $\mathcal{A}$  penetrating  $S$ , for which case we have  $d_i < 0$  for  $i = 1, 2, 3$  and  $d_i > 0$  for  $i = 4, 5, 6 > 0$ . **Fig. 7(c)** depicts  $\mathcal{A}$  being completely past  $S$ , for which case we have  $d_i < 0$  for  $i = 1, 2, \dots, 6$ . We will only encounter scenarios (a) and (b) where the center of mass (COM) point is always in the half-space of the plane, thus  $d_i < 0$ , for any  $i \in (1, 2, \dots, n)$  is indicative that contact has taken place. We summarize this as follows:

**Theorem 1.** If the  $\perp$  distance  $d_i > 0$  for  $i = 1, 2, \dots, n$  (Eq. (1)) between all vertexes  $\mathbf{v}_i$  for  $i = 1, 2, \dots, n$  of a polyhedron  $\mathcal{A}$  and  $S(\mathbf{n}, \mathbf{c})$ , then there is no contact between  $\mathcal{A}$  and  $S$ .

When applied to two polyhedra Theorem 1 is termed the separating plane (SP) method which was first described by Cundall [22]. The SP method reduces the expensive object-to-object contact detection problem to a less expensive plane-to-object contact problem. The aim is to find a plane between the two polyhedra that satisfies Theorem 1. If such a plane is found the two objects cannot be in contact. Many algorithms are based on this approach [9,22]. However, they involve finding a SP by an iterative procedure, often minimizing a distance function [9], which is not suitable to the SIMD nature of the GPU. Furthermore, to minimize memory transactions our algorithms do not require a separate stage for finding points, an approach that is typical in numerous implementations [9,18,19]. It is computationally more efficient to do additional arithmetic operations rather than additional memory transactions on the GPU.

### 3.4. Polyhedron–Polyhedron contact algorithm

As discussed in Section 3.2, detecting vertex–face contact is computationally cheaper than edge–edge contact. Given two polyhedra  $\mathcal{A}$  and  $\mathcal{B}$ , we just need to apply Eq. (1) to the vertex set  $\mathbf{v}_j^{\mathcal{B}}$  and half-planes  $P_i^{\mathcal{A}}(x, y, z)$  and the vertex set  $\mathbf{v}_i^{\mathcal{A}}$  and half-planes  $P_j^{\mathcal{B}}(x, y, z)$  to determine if there is Type 1 contact. This is computationally efficient on the GPU, due to the fact that by definition the half-planes  $P_i(x, y, z)$  subtended by the faces, partition space into two distinct regions. Hence we can use the result of Theorem 1 to check if a SP exists. If a SP does not exist, then we check if a vertex has penetrated all half-spaces, which implies that it is contained within the other polyhedron and therefore it is a contacting vertex. If there is no SP or contact vertices then we check for Type 2 contact.

#### 3.4.1. Edge–edge contact detection

Recall that for Type 2 contact we do not search for a SP we rather search for penetration between 2 edges and use the fact that if these edges are not penetrating there must be a SP and hence the polyhedra cannot be in contact. This is much cheaper computationally than searching for a SP between edges. Consider Fig. 8(a) which depicts a typical scenario that will be a candidate for edge contact and Fig. 8(b) which depicts edge contact.

From Fig. 8(a) we use the parametric equations to represent the edges:

$$\mathbf{PE}_{\mathcal{A}} = \mathbf{E}_{\mathcal{A}}^0 + d_{\mathcal{A}} \mathbf{E}_{\mathcal{A}}^{\text{Dir}} \quad (2)$$

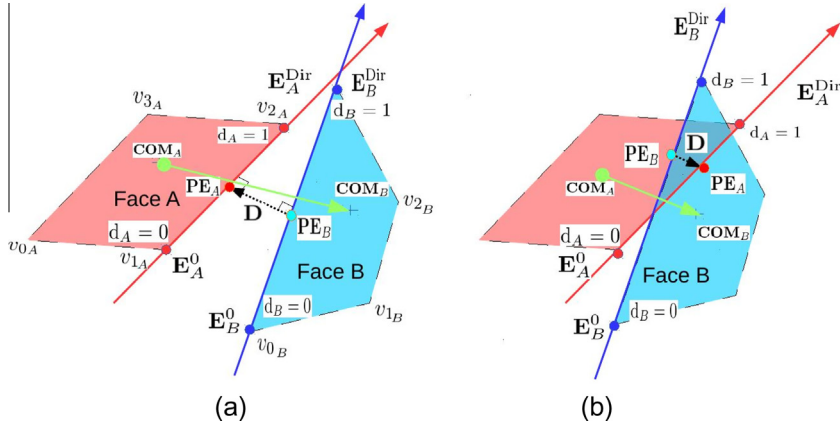


**Fig. 8.** (a) Non penetrating Type 2 contact, (b) Penetrating Type 2 contact.

$$\mathbf{PE}_B = \mathbf{E}_B^0 + d_B \mathbf{E}_B^{\text{Dir}} \quad (3)$$

where  $\mathbf{E}_K^0$  is a vertex  $\mathbf{v}_i$  on the edge,  $\mathbf{E}_K^{\text{Dir}} = \mathbf{v}_j - \mathbf{v}_i$  is the direction of the edge where  $\mathbf{v}_j$  is the other vertex on the edge.  $d_A$  and  $d_B$  are the scalar parameters for which we solve. We find  $d_A$  and  $d_B$  that yields the shortest distance between the two edges using the fact that the shortest distance between two edges is a vector  $\mathbf{D} = \mathbf{PE}_A - \mathbf{PE}_B$  that is perpendicular to both edges as indicated in Fig. 8(a).

$$d_A = \text{detJinv} * [(\mathbf{E}_B^{\text{Dir}} \cdot \mathbf{E}_B^{\text{Dir}}) * (\mathbf{E}_A^{\text{Dir}} \cdot (\mathbf{E}_A^0 - \mathbf{E}_B^0)) - (\mathbf{E}_A^{\text{Dir}} \cdot \mathbf{E}_B^{\text{Dir}}) * (\mathbf{E}_B^{\text{Dir}} \cdot (\mathbf{E}_A^0 - \mathbf{E}_B^0))] \quad (4)$$

$$d_B = \text{detJinv} * [(\mathbf{E}_A^{\text{Dir}} \cdot \mathbf{E}_B^{\text{Dir}}) * (\mathbf{E}_A^{\text{Dir}} \cdot (\mathbf{E}_A^0 - \mathbf{E}_B^0)) - (\mathbf{E}_A^{\text{Dir}} \cdot \mathbf{E}_A^{\text{Dir}}) * (\mathbf{E}_B^{\text{Dir}} \cdot (\mathbf{E}_A^0 - \mathbf{E}_B^0))] \quad (5)$$

where  $\text{detJinv} = 1 / [(\mathbf{E}_A^{\text{Dir}} \cdot \mathbf{E}_B^{\text{Dir}}) * (\mathbf{E}_A^{\text{Dir}} \cdot (\mathbf{E}_A^0 - \mathbf{E}_B^0)) - (\mathbf{E}_A^{\text{Dir}} \cdot \mathbf{E}_A^{\text{Dir}}) * (\mathbf{E}_B^{\text{Dir}} \cdot \mathbf{E}_B^{\text{Dir}})]$ . Fig. 9 describes our algorithm for polyhedra contact detection.

Line 1 is a loop over all faces of polyhedron  $\mathcal{B}$  to search for a SP. Line 2 is a flag, used to exit the loop once we find a SP. Line 3 is a loop over the vertices of polyhedron  $\mathcal{A}$  and line 4 is the application of Eq. (1) to each vertex. Line 6 sets the flag to false if there is no SP, while Line 7 increments a counter that stores how many faces a vertex has intersected. Line 8 is an exit condition as a SP has been found. Lines 9–19 check for a Type 1 collision by checking if the counter for a vertex equals the number of faces indicating the vertex is inside polyhedron  $\mathcal{B}$  and therefore a contact point. Line 18 is an exit condition if contact points have been found. If there is no SP or contact points then Lines 1–19 are repeated with the faces of polyhedron  $\mathcal{A}$ . If the faces of polyhedron  $\mathcal{A}$  does not yield a SP or contact point then we check for Type 2 contact (Lines 21–35). We also sort our data based on spatial location which increases cache hits and improves performance. This is described in the code BLAZE-DEM [16] developed by the authors.

### 3.5. World polyhedron contact

Eq. (1) treats a surface as an infinite plane. We are however interested in finite surfaces, as illustrated in Fig. 10(a). We thus need to check that a vertex that is reported to be penetrating the plane is actually contained on the surface of the polygon described by that plane. We do this by tessellating the surface into triangles using the vectors  $L_i$ ,  $i = 1, 2, \dots, m$  as described in Fig. 10(b). The area  $A_i$ ,  $i = 1, 2, \dots, m$  for each triangle is calculated using the norm of the cross-product of two vectors describing the edges of the triangle. If the vertex is indeed contained within the finite surface, then  $\sum_i^M A_i$  will equal the total area of the surface.

We summarize this result as:

**Theorem 2.** If the  $\perp$  distance ( $d_i, i = 1, 2, \dots, k$ )  $> 0$  (Eq. (1)) between any vertex ( $\mathbf{v}_i, i = 1, 2, \dots, k$ ) of a polyhedral object  $\mathcal{A}$  and half-space  $S(\mathbf{n}, \mathbf{c}) < 0$  then there is contact between  $\mathcal{A}$  and  $S$ , provided the vertex is contained within the surface.

Typical world geometry consists of many surfaces. Thus, our algorithm must provide a quick rejection of surfaces with which the particle cannot be in contact. In addition, the algorithm must detect and identify contact in an efficient manner so that we can reduce thread divergence which has a major impact on parallel performance. Fig. 11 describes our contact detection algorithm for polyhedron-planar surface contact.

Lines 1–2 are heuristics. Line 1 checks if the COM point is on the correct side of the surface. Line 2 uses the radius from the COM point to the vertex furthest away to check if there is an intersection, since this sphere contains the entire polyhedron. If this sphere does not intersect with the surface, then neither does the polyhedron. These heuristics are computationally cheap

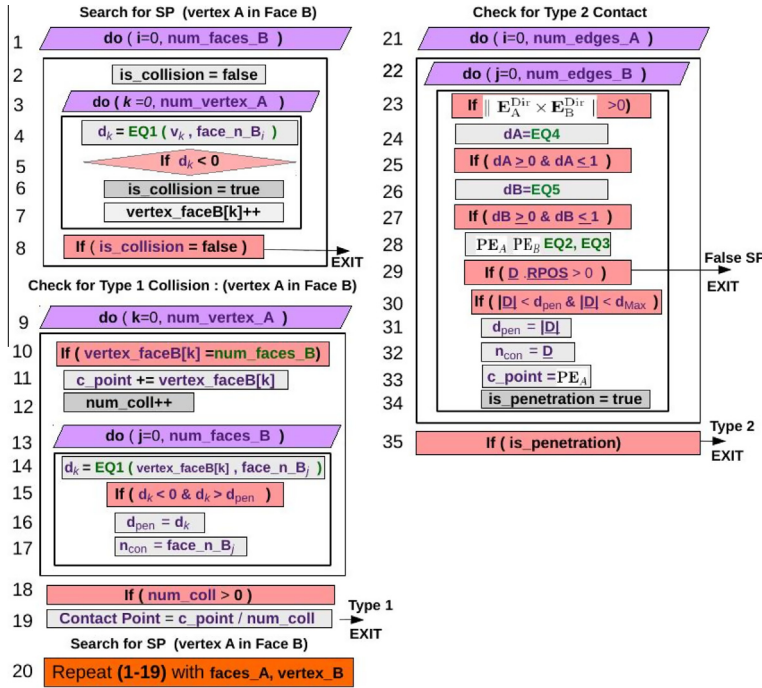


**Fig. 9.** Algorithm 1: Polyhedron–Polyhedron contact detection.

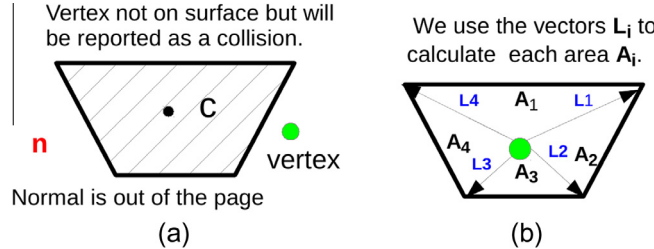


**Fig. 10.** Check for surface collisions.

and can be executed in parallel, thus quickly eliminating surfaces with which the particle cannot be colliding with. If a particle passes the heuristics, then we apply Eq. (1) to all vertices of the particle (Line 4). If a vertex satisfies **Theorem 2** then we increment the counter that we use to classify the collision (Line 5). The contact point **PC** is considered to be the average of the vertices which are in contact with the surface  $\mathbf{PC} = (\sum_{k=0}^m \mathbf{v}_k)/m$ , where  $m$  is the number of contact points. The penetration distance  $d_{\text{pen}}$  is the averaged of  $d_i$  for all penetrating vertices.

#### 4. Contact resolution

The total force experienced by a particle during contact is given by  $\mathbf{F} = \mathbf{F}_N + \mathbf{F}_T$ , where  $\mathbf{F}_N$  and  $\mathbf{F}_T$  represent the normal and tangential forces respectively. Consider Fig. 12(a) which depicts two contacting particles. We use a penalty approach in that the normal force has a dependance on the amount of interpenetration between 2 particles. Fig. 12(b) depicts the scenario we simulate in Section 4.1. Note: the cube is stationary with the octahedron given an initial velocity towards the cube which we denote “downwards”.

##### 4.1. Normal force

###### 4.1.1. Restorative force

The normal force consists of an elastic  $\mathbf{F}_N^{\text{elastic}}$  and dissipative part  $\mathbf{F}_N^{\text{diss}}$ . The elastic contribution is represented using a non-linear spring that acts to move particles out of contact.

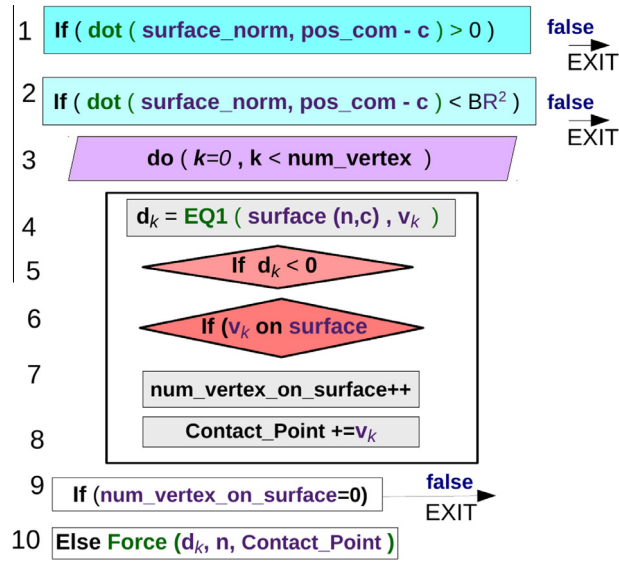


Fig. 11. Algorithm 2: Polyhedra-World.

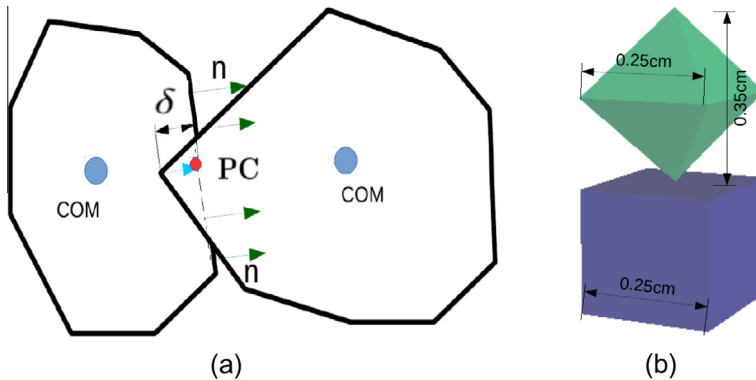


Fig. 12. (a) Polyhedral particle contact model and (b) Simulation scenario for Section 4.

$$\mathbf{F}_N^{\text{elastic}} = (K_r \delta^{\frac{3}{2}}) \mathbf{n} \quad (6)$$

where  $\delta = d_{pen}$  is the penetration depth and  $\mathbf{n}$  the contact normal. The spring stiffness  $K_r$  can be chosen using the material properties as defined by Bell et al. [15] or manually tuned to yield the desired response. For this study we manually tune parameters as we are not simulating a real material and only wish to verify our contact algorithms. (Note: we use cm as the unit of length). The bounding radius for the simulations depicted in Figs. 13–24 is 0.25 cm. The maximum allowed penetration depth is 5% of this which is 0.0125 cm.

Fig. 13 shows how the penetration depth varies with different incident velocities for a particle undergoing a head-on elastic collision. We see a parabolic curve, which becomes sharper as velocity increases which is the expected result of Eq. (6). This information can be used to tune  $K_r$  for a range of velocities that is observed for a typical GM simulation based on experimental or simulation data, so that the desired maximum penetration depth, or a bound on the contact time can be obtained.

Fig. 14 shows how  $\mathbf{F}_N^{\text{elastic}}$  varies as a function of the penetration depth for an incident velocity of  $v = 2 \text{ m s}^{-1}$ . We see a non-linear dependence on penetration depth for both loading and unloading as expected. We also see that the curves for both stages are identical which is further indication that our algorithms are implemented correctly.

An important test of our contact detection and resolution algorithms is that for a head-on elastic collision kinetic energy must be conserved. Fig. 15 shows how the velocity varies during contact. We see that for all incident velocities the pre and post collision velocities are the same.

Table 1 gives us a quantitative estimate on the accuracy of our code by analyzing the pre and post collision velocities which must be conserved. Here,  $\mathbf{V}$  indicates the expected result and  $\mathbf{V}'$  the numerically computed result. We see excellent agreement with a maximum difference of 0.33%.

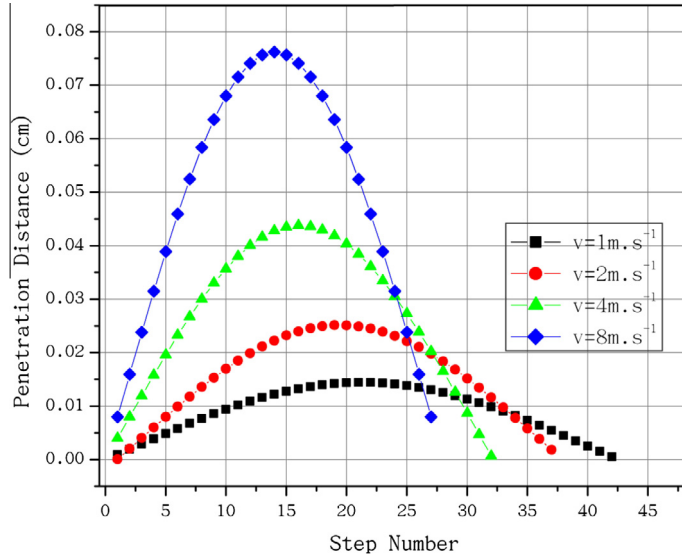


Fig. 13. Penetration distance as a function of time step for a head-on elastic collision. ( $K_r = 1 \times 10^9$ , step size =  $10^{-5}$ ).

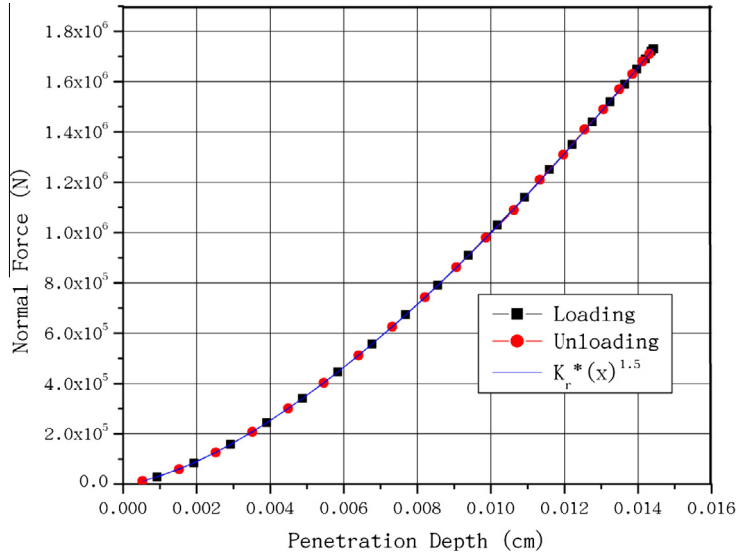


Fig. 14.  $F_N^{\text{elastic}}$  as function of penetration depth for a head-on elastic collision. ( $K_r = 1 \times 10^9$ , step size =  $10^{-5}$ ).

#### 4.1.2. Dissipative force

Dissipation during contact is given by:

$$\mathbf{F}_N^{\text{diss}} = -K_D \delta^\gamma \mathbf{v}_{\text{rel}} \mathbf{n}, \quad (7)$$

where  $K_D$  is the damping coefficient and  $\mathbf{v}_{\text{rel}} = ((\mathbf{v}_1 - \mathbf{v}_2) \cdot \mathbf{n}) \mathbf{n}$  is the relative normal translational velocity.  $\gamma = \frac{1}{2}$  was found to match experimental data the best by Bell et al. [15], as the energy dissipation increases with increasing impact velocity. Fig. 16 shows the force hysteresis for  $F_N$ . We see that adding energy dissipation results in an elliptical shape for the force that is asymmetric. This shape is consistent with that of other authors [18]. We firstly see that at the start of loading (0 penetration distance) the force points upwards opposing the downwards motion of the octahedron, which is a result of the dissipative force as there is no elastic contribution. The dissipative force once again exceeds the elastic force contribution towards the end of the unloading stage resulting in a negative total force that is decelerating the body which is now moving in an upwards direction. This negative force might seem non-physical but none of authors [15,23] have reported non-physical effects such as the particle being attracted to the surface during contact. Nevertheless we verify the realism of the force model for a particle in free fall as illustrated in Section 4.1.3.

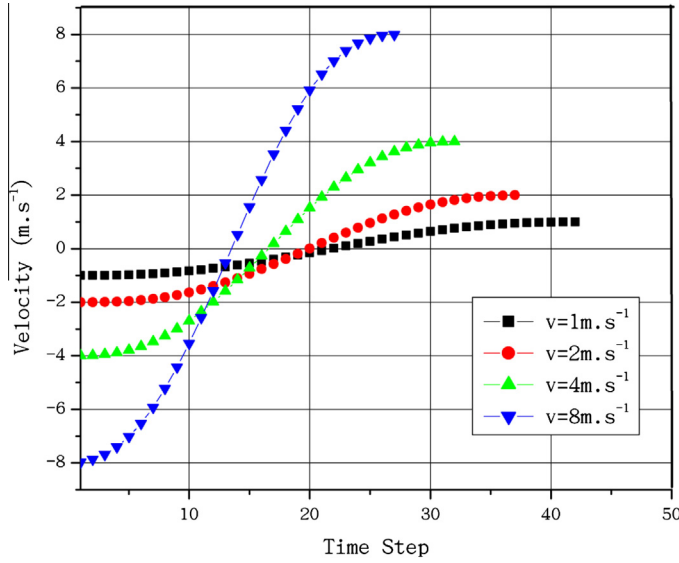


**Fig. 15.** Velocity as a function of time step for a head-on elastic collision. ( $K_r = 1 \times 10^9$ , step size =  $10^{-5}$ ).

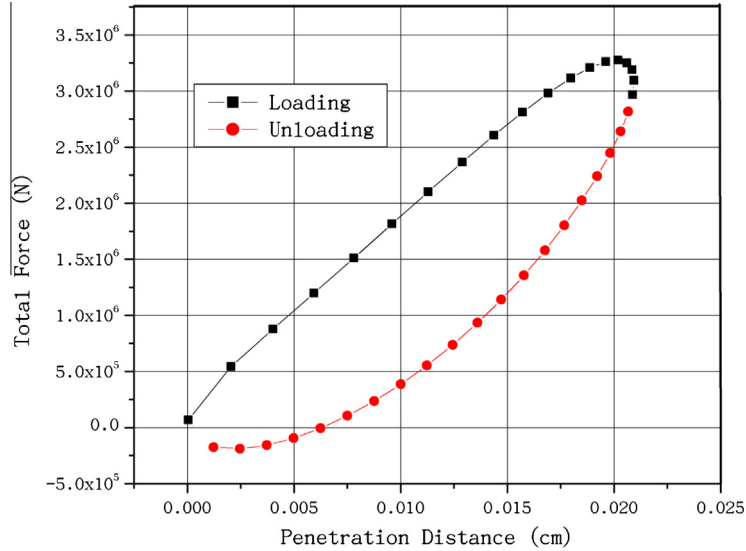


**Fig. 16.** Normal force as a function of penetration depth for a head-on in-elastic collision. ( $K_r = 1 \times 10^9$ ,  $K_D = 5 \times 10^4$ , step size =  $10^{-5}$ ,  $v = 2 \text{ m s}^{-1}$ ).

Fig. 17 shows the difference between  $\|\mathbf{F}_N^{elastic}\|$  and  $\|\mathbf{F}_N^{diss}\|$  as a function of velocity (vertical lines indicate the onset of contact). We firstly see that for high initial velocity collisions that  $\mathbf{F}_N^{diss}$  dominates at the start and end of the collision, resulting in a large dissipation of energy. This is consistent with experimental data [15] and explains the negative total force in Fig. 16 at the initial stages of contact. We also see that the contact time increases with decreasing velocity, while there is effectively no damping for small velocity impacts that occur when the particle is in persistent contact with the surface.

#### 4.1.3. Contact evaluation for particle in free fall

Fig. 18 shows the evolution of the position for a particle dropped from rest undergoing inelastic contact with a surface. We see the particle undergoing a number of contacts with the surface before reaching an equilibrium as expected.

Fig. 19 shows the corresponding velocity for Fig. 18. We see that the velocity also reaches an equilibrium as expected.

#### 4.2. Tangential force

The tangential force is given by:

$$\mathbf{F}_T = -\min [\mu \|\mathbf{F}_N\|, K_T \|\mathbf{v}_T\|] \left( \frac{\mathbf{v}_T}{\|\mathbf{v}_T\|} \right) \quad (8)$$

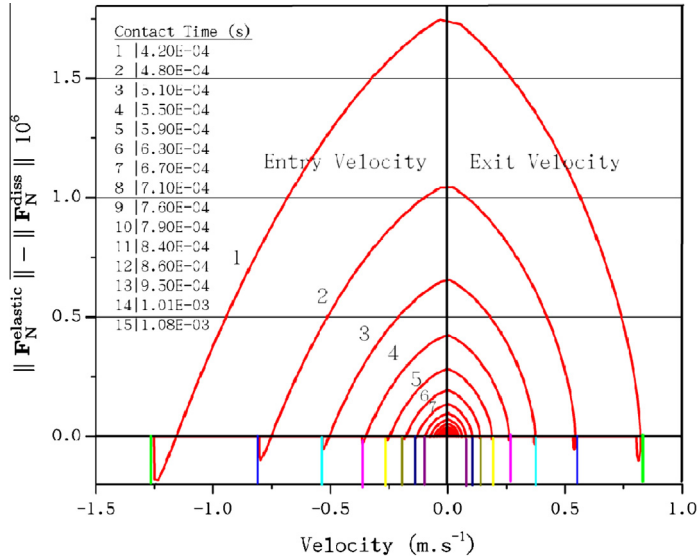


Fig. 17.  $\|F_N^{\text{elastic}}\| - \|F_N^{\text{diss}}\|$  vs velocity ( $K_r = 1 \times 10^9$ ,  $K_D = 5 \times 10^4$ , step size =  $10^{-5}$ ).

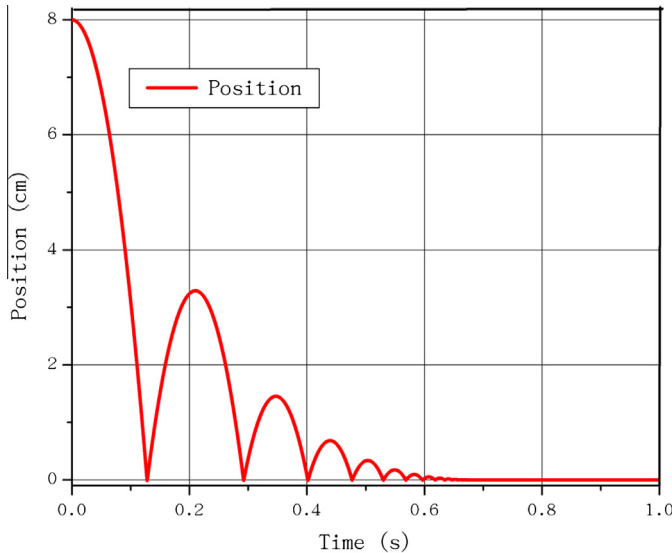


Fig. 18. Position vs Time ( $K_r = 1 \times 10^9$ ,  $K_D = 5 \times 10^4$ , step size =  $10^{-5}$ ).

where  $\mathbf{v}_T = (\mathbf{v}_R - (\mathbf{v}_R \cdot \bar{\mathbf{n}}_s))\bar{\mathbf{n}}_s$  is the relative tangential velocity,  $\mu$  the coefficient of friction and  $K_T$  the viscous damping coefficient [15]. The values for  $\mu$  and  $K_T$  should be such that  $K_T$  affects oblique impacts while  $\mu$  affects rolling/sliding contact. To illustrate this we simulate the motion of the octagon shaped particle with an initial velocity of  $2\text{ m s}^{-1}$  in the tangential direction and  $-0.5\text{ m s}^{-1}$  in the normal direction (“downwards”) in a gravity field initially placed  $0.75\text{ cm}$  above the surface (no rotation). Fig. 20 shows the evolution particle position and tangential velocity with time. In Fig. 20(a) we see that the particle undergoes 4 oblique collisions with the surface before the rebound height becomes sufficiently small such that the particle can be considered to be moving on the surface. Fig. 20(b) shows the corresponding tangential velocity which has two distinct patterns. The velocity firstly decreases in steps for  $t < 0.055$  which is indicative of viscous damping and thereafter it decreases in a linear fashion which corresponds to a constant frictional force.

Fig. 21 shows the tangential force as a function of velocity, we see that indeed for high velocity oblique collisions  $K_T\|\mathbf{v}_T\|$  dominates while for low velocity collisions  $\mu\|F_N\|$  dominates.

In addition to translation forces a particle also experiences a torque as a result of contact given by:

$$\Gamma = (\mathbf{r} \times \mathbf{F}) \quad (9)$$

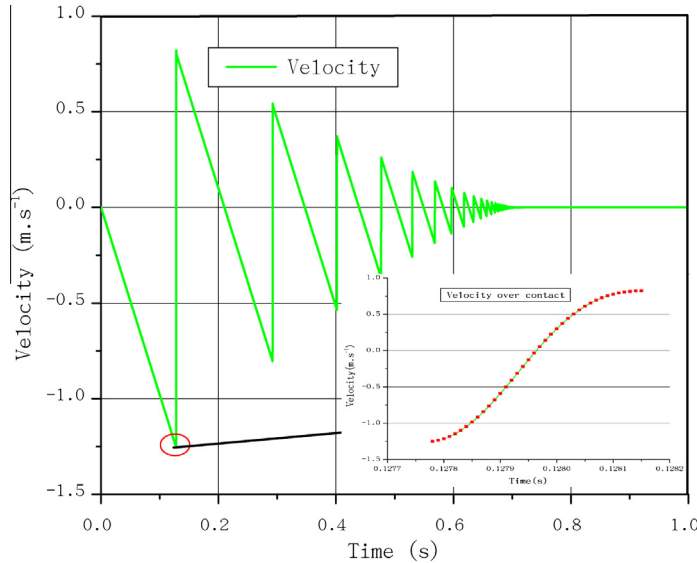


**Fig. 19.** Velocity vs Time ( $K_r = 1 \times 10^9$ ,  $K_D = 5 \times 10^4$ , step size =  $10^{-5}$ ).

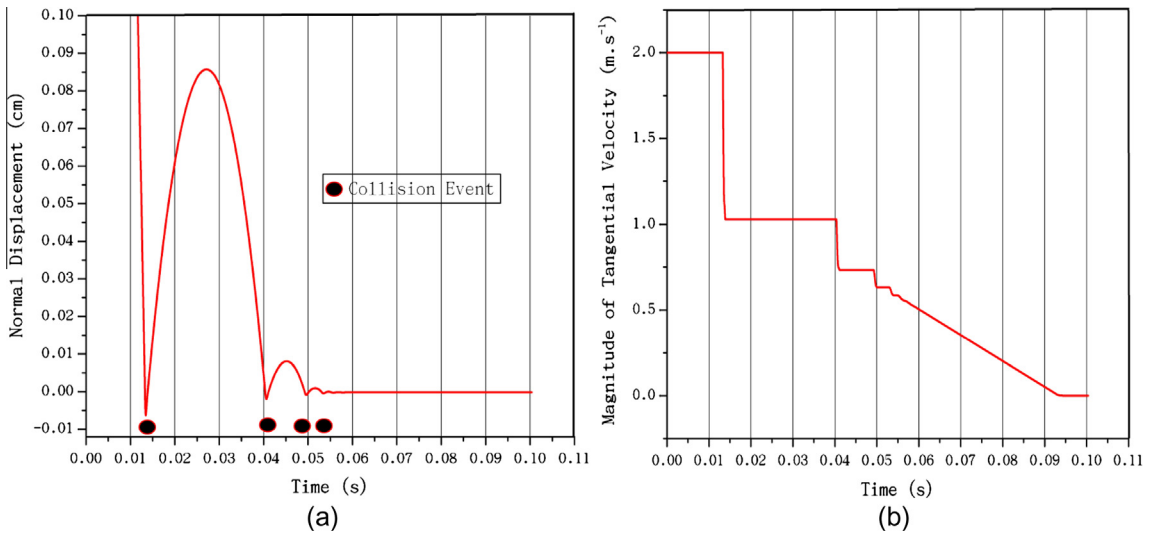


**Fig. 20.** (a) Position vs Time and (b) Velocity vs Time ( $K_r = 1 \times 10^9$ ,  $K_D = 2 \times 10^5$ ,  $\mu = 1.54$ ,  $K_T = 4 \times 10^3$ , step size =  $10^{-5}$ ).

where  $\mathbf{r}$  is the vector from the COM to the contact point  $\mathbf{PC}(x, y, z)$ .

#### 4.3. Numerical integration

We use the explicit velocity Verlet algorithm, which is second order accurate, to obtain the position  $\mathbf{x}$  and velocity  $\mathbf{v}$  of a particle  $i$  at time  $k$ :

$$\mathbf{x}_k^i = \left[ \mathbf{x}_{k-1}^i + \mathbf{v}_{k-1}^i \Delta t + \frac{1}{2} \mathbf{a}_{k-1}^i \Delta t^2 \right] \quad (10)$$

$$\mathbf{v}_k^i = \left[ \mathbf{v}_{k-1}^i + \frac{1}{2} (\mathbf{a}_{k-1}^i + \mathbf{a}_k^i) \Delta t \right] \quad (11)$$

The acceleration  $\mathbf{a}$  at time  $k$  is given by  $\mathbf{a}_k = \frac{\mathbf{F}_{\text{net}}^k}{m}$  where  $\mathbf{F}_{\text{net}}^k = \sum_{j=1}^L \mathbf{F}_k^{ij}$  is the sum of all  $L$  contact forces experienced by the particle. To ensure that the integration scheme we employ behaves as expected we simulate the motion of a system of particles falling under the influence of gravity for 1 s onto a planar surface. Fig. 23 shows the error in the total energy of the

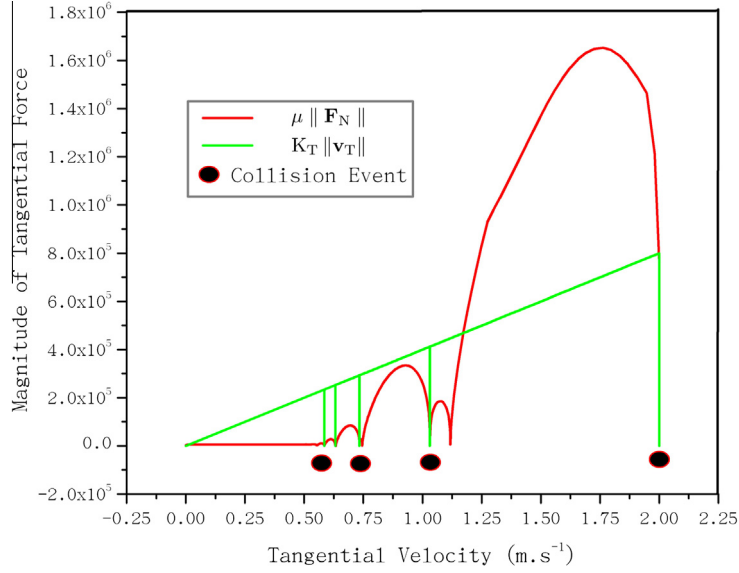


**Fig. 21.**  $\|F_T\|$  vs Tangential Velocity ( $K_r = 1 \times 10^9$ ,  $K_D = 2 \times 10^5$ ,  $\mu = 1.54$ ,  $K_T = 4 \times 10^3$ , step size =  $10^{-5}$ ).

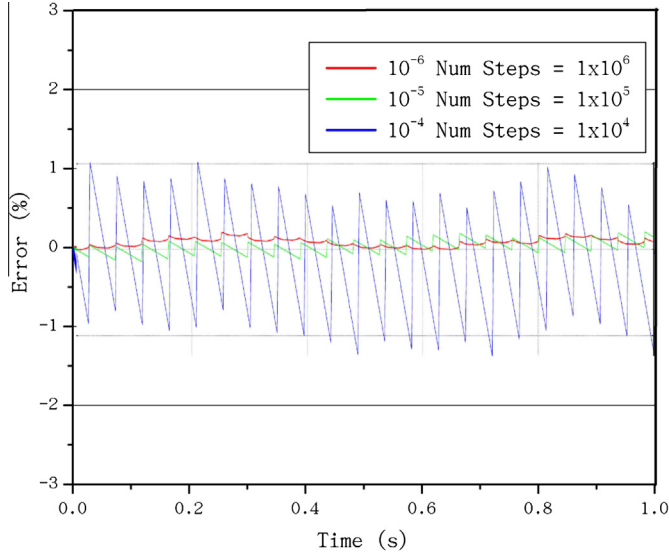


**Fig. 22.** Error in Energy Conservation.

system for various time-steps. We firstly see the error remains within a bound for the time-steps sampled and decreases with a smaller time-step as expected. While a time step size of  $10^{-5}$  is satisfactory we will use a time step size of  $10^{-6}$  for our simulation examples as it is typically used in DEM simulations by other authors and will allow for unbiased comparisons.

#### 4.3.1. Angular integration

The angular velocity  $\omega$  of particle  $i$  at time  $k$  is obtained using the forward Euler integration scheme.

$$\omega_k = \omega_{k-1} + \alpha_k^{\text{ang}} \Delta t. \quad (12)$$

The angular acceleration  $\alpha^{\text{ang}}$  at time  $k$  is given by  $\alpha_k^{\text{ang}} = \mathbf{I}_k^{-1} \Gamma_k^{\text{net}}$  where  $\Gamma_k^{\text{net}} = \sum_{j=1}^L \Gamma_j^{ij}$  is the sum of all  $L$  body contact torques experienced by particle  $i$  as given in Eq. (9) and  $\mathbf{I}_k$  the inertia tensor at time  $k$ . Quaternions have minimal storage requirements and are thus well suited to the GPU, and they are also more robust than other representations such as Euler angles [24]. The orientation of a particle is represented by a unit quaternion  $\mathbf{q}\{w, x, y, z\} = \{1, 0, 0, 0\}$ , where  $w$  is an angle

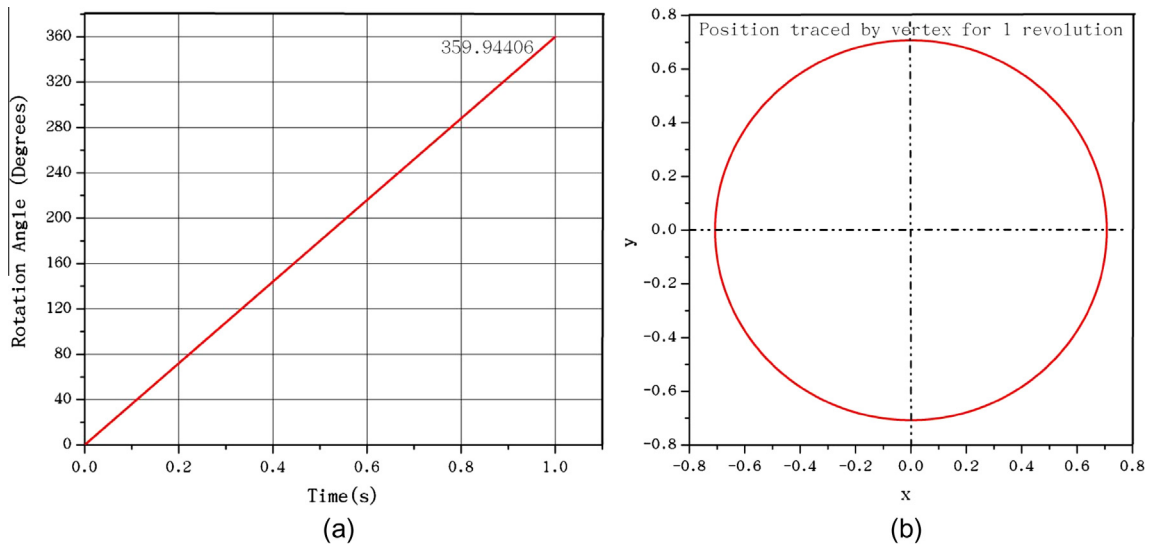


**Fig. 23.** Results of angular integration depicting (a) angular displacement (rotation angle) as a function of time and (b) the position of a vertex on the rotating cube.

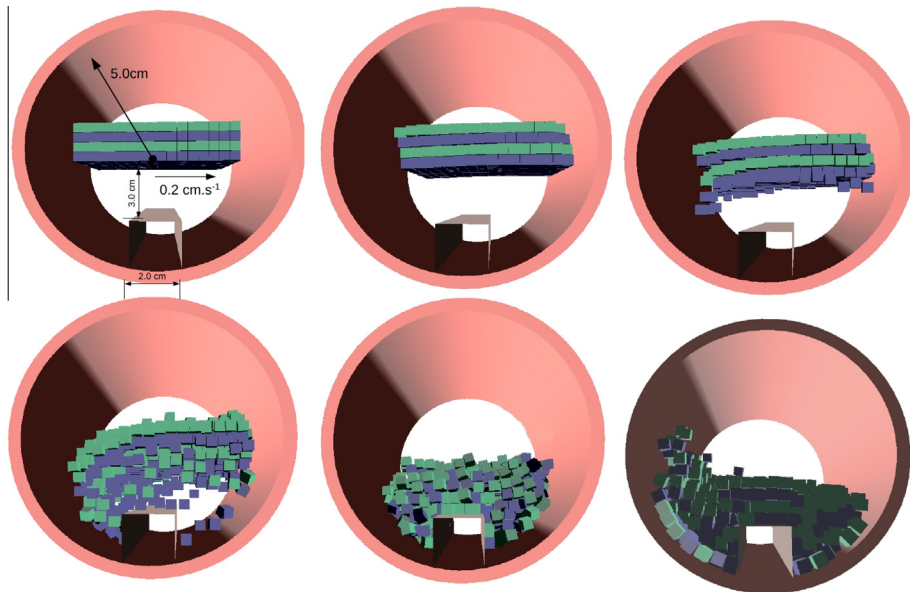


**Fig. 24.** Packing of dynamic cubes in a drum.

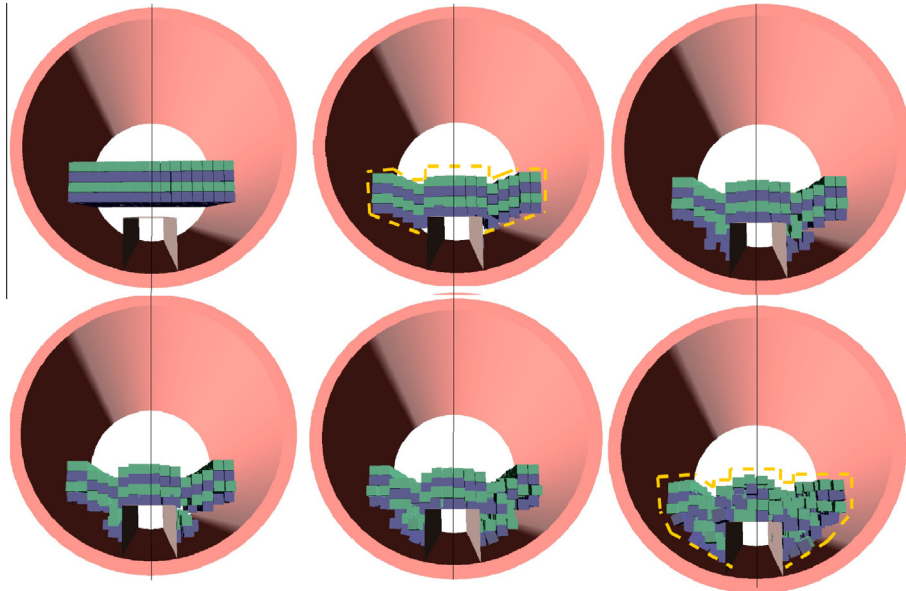
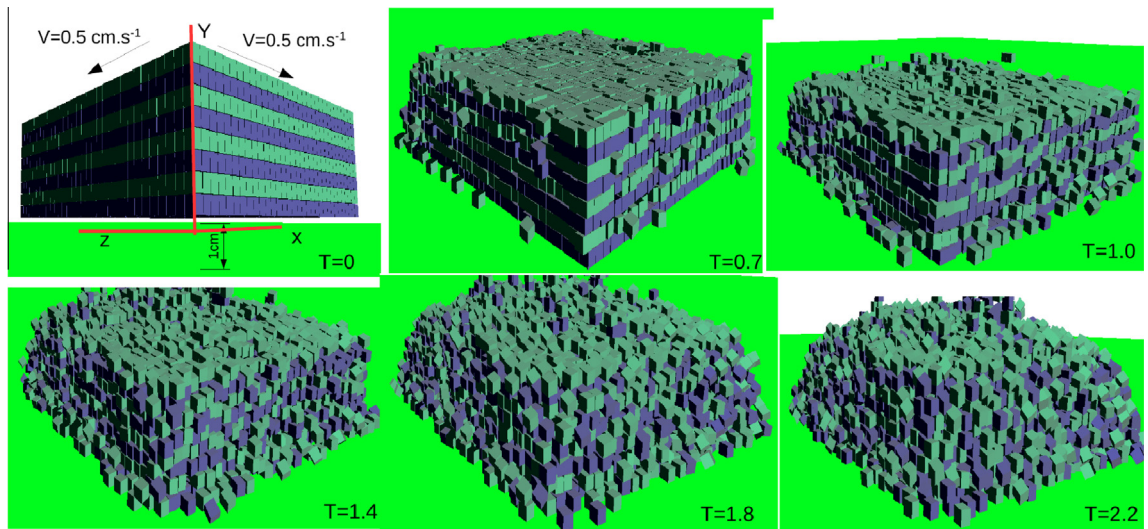
**Table 1**  
Analysis of particle velocities for a head-on elastic collision.

$\mathbf{V}$ ( $\text{m s}^{-1}$ )	$\mathbf{V}'$ ( $\text{m s}^{-1}$ )	% Diff
0.062500	0.062582	-0.1312
0.125000	0.125249	-0.1992
0.250000	0.250152	-0.0608
0.500000	0.501799	-0.3595
1.000000	0.996799	0.32010
2.000000	1.997261	0.13695
4.000000	4.013109	-0.32772

**Table 2**

Parameters used in simulations for non-linear force model.

Parameter	$\Delta t$	$K_r$	$K_d$	$\mu$	$K_t$
Value	$10^{-6}$	$1 \times 10^8$	$5 \times 10^3$	0.154	$4 \times 10^2$

**Fig. 25.** Packing of cubes in a drum (symmetric).**Fig. 26.** Gravity packing simulation for performance benchmarking.

$[-1 : 1]$  and  $(x, y, z)$  the axis of rotation. The relationship between a quaternion and axis angle representation  $(\theta, x_1, y_1, z_1)$  is given by:

$$\mathbf{q} = \{\cos(\theta/2), x_1 \sin(\theta/2), y_1 \sin(\theta/2), z_1 \sin(\theta/2)\}. \quad (13)$$

Given an angular velocity vector  $\omega$  the quaternion representing that rotation is given by:

$$\Delta \mathbf{q} = \left\{ \cos(\|\omega_k\|), \sin(\|\omega_k\|) \frac{\omega_k}{\|\omega_k\|} \right\}. \quad (14)$$

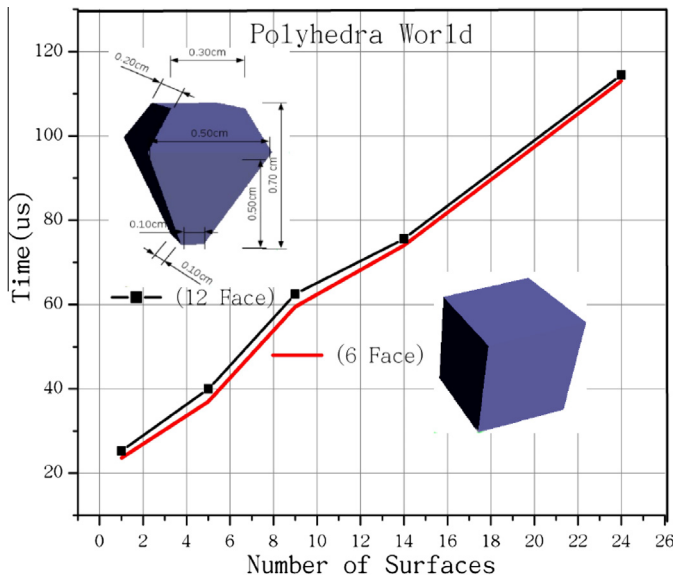


Fig. 27. Computational scaling of World-Polyhedron collision detection with world surfaces.

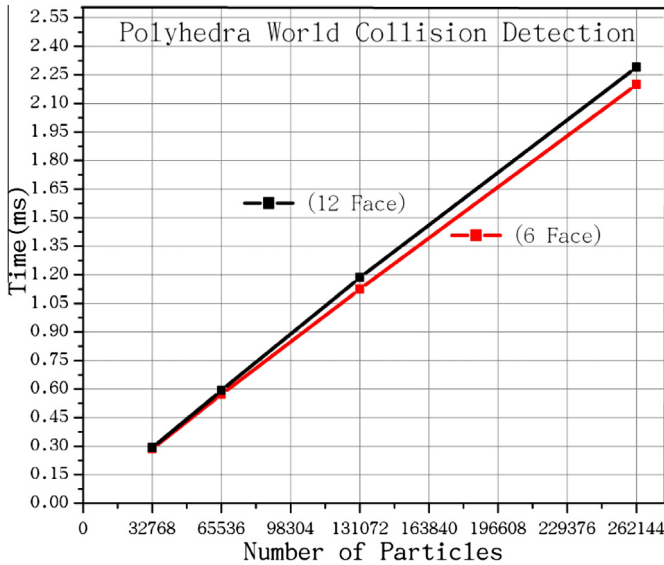


Fig. 28. Effect of particle shape (number of faces) on the computational cost of collision detection.

The evolution of the angular orientation of the particle is just a multiplication [25] between the current quaternion  $\mathbf{q}_{k-1}$  of a particle with  $\Delta\mathbf{q}$ :

$$\mathbf{q}_k = \mathbf{q}_{k-1} \times \Delta\mathbf{q}. \quad (15)$$

To verify that rotation using quaternions on the GPU is correct, we simulate a cube spinning with a constant velocity of  $(1, 0, 0)$  rads $^{-1}$  with a step-size of  $10^{-5}$ . Fig. 23(a) shows the angular displacement as a function of time. We see that it varies in a linear fashion as expected with the total angle of rotation at the end of  $1s = 359.94406$  giving an error of 0.015% which is within error tolerances.

Fig. 23(b) shows how the position of a vertex on the cube varies with time which gives an indication if any shearing of the shape occurs. We see a perfect circular path which implies that there is no shearing of shape occurring. Note: in Eq. (15) as  $\omega_k \rightarrow 0$ ,  $\Delta\mathbf{q} \rightarrow \{1, 0, 0, 0\}$  which leaves the orientation unchanged and hence does not result in numerical difficulties.

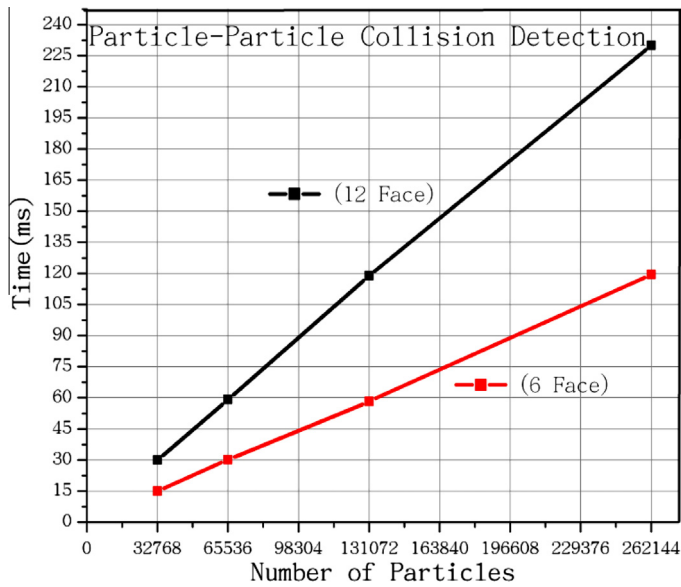


**Fig. 29.** Scaling of Polyhedron–Polyhedron collision detection with number of particles (N) for different polyhedra.

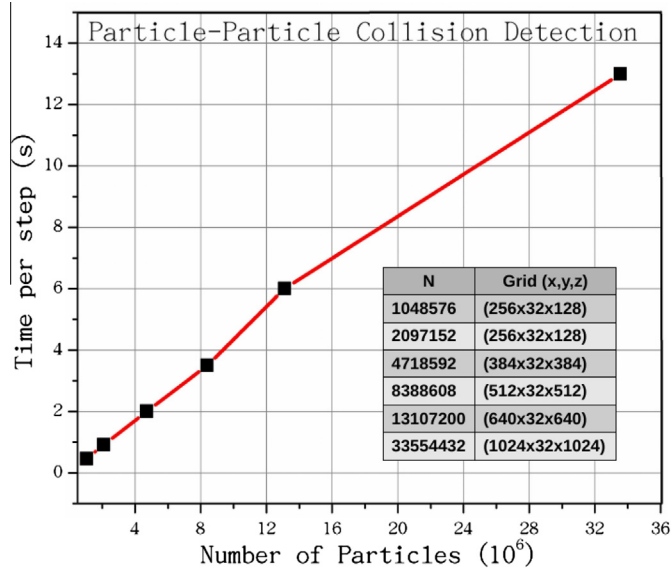


**Fig. 30.** Scaling of Polyhedron–Polyhedron collision detection with number of particles (N) for the six face polyhedron.

## 5. Numerical simulation

All simulations are done using a NVIDIA Quadro K6000 GPU (30720 physical threads) on an Intel i7 3.5 GHZ Extreme Edition CPU with 32 GB of RAM under OpenSuse Linux 13.1. The values for all parameters are given in [Table 2](#).

### 5.1. Polyhedra in a drum

To verify that our algorithms correctly detects collisions, we model the gravity packing of 1024 tightly packed cubes (edge length 0.50 cm) in a drum with a blade as depicted in [Fig. 24](#). Notice that all the cubes are given an initial velocity of  $0.2\text{cm s}^{-1}$  to the right. We see that the particles take the shape of the container with the faces resting on the cylinder and around the obstacle (blade) which is what we expect. This gives as a qualitative indication that our algorithms correctly detect collisions.

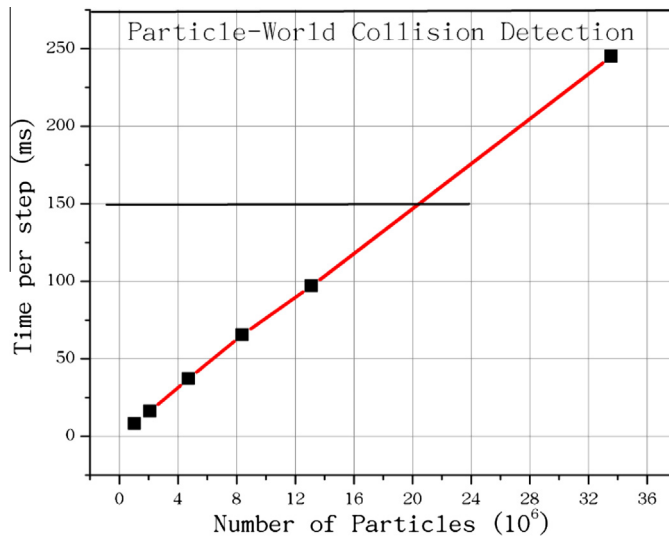


Fig. 31. Scaling of Polyhedron-World algorithm with number of particles (N).

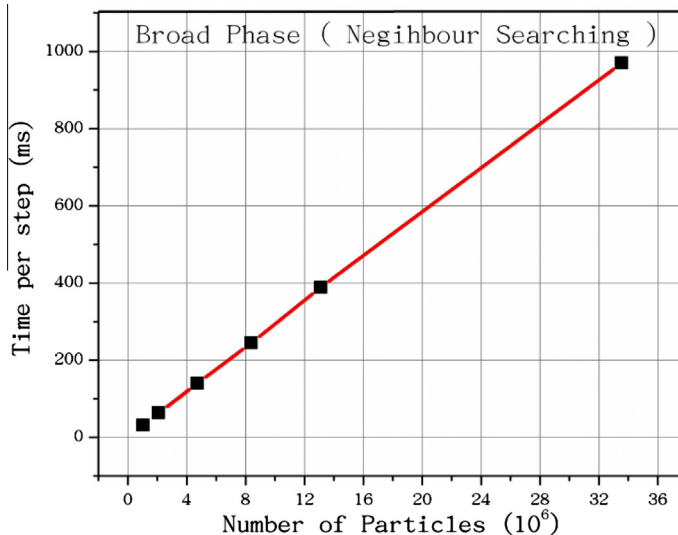
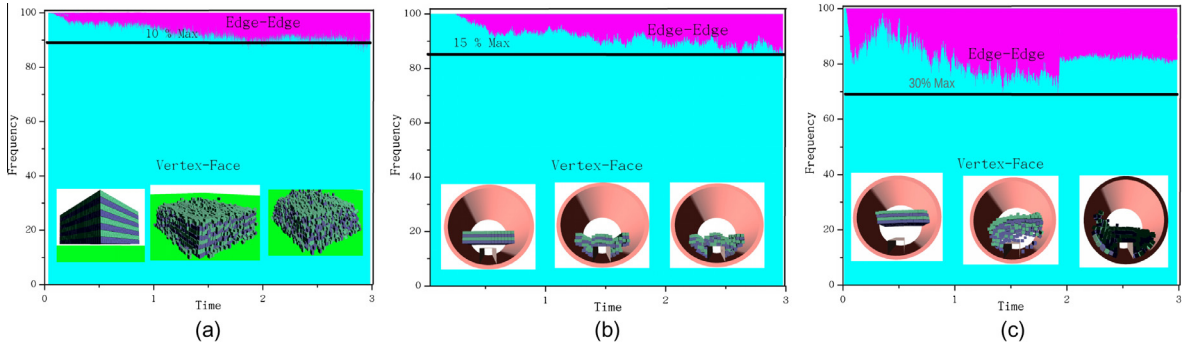


Fig. 32. Scaling of Broad-Phase algorithm with number of particles (N).

**Table 3**  
Comparison to other GPU codes (mono sized particles) \*Kepler class GPU.

Author	Shape	N particles	C Number
Harida et al. [25]	Clumped	$1.64 \times 10^4$	$0.66 \times 10^6$
Longmore et al. [23]	Clumped	$2.56 \times 10^5$	$1.49 \times 10^6$
This paper	*Poly	$34 \times 10^6$	$2.62 \times 10^6$
Radake et al. [6,26]	*Sphere	$20 \times 10^6$	$20 \times 10^6$
Govender et al. [12,27]	*Sphere	$50 \times 10^6$	$55 \times 10^6$

In Fig. 25 the cubes are arranged symmetrically in the drum with an initial height of 1 cm above the horizontal section of the blade.). The cubes fall under the influence of gravity only (zero initial velocity). We see that the packing is symmetric, which is what we expect, further validating our algorithms.



**Fig. 33.** Frequency plot of the collision type against simulation type for (a) gravity packing problem, (b) gravity packing in drum without initial velocity, (c) gravity packing in drum with initial velocity.

### 5.2. Scaling with particle shape

To further evaluate the performance of our algorithms, we simulate the motion of tightly packed identical cubes (edge length 0.50 cm) arranged in a rectangular grid, falling under the influence of gravity with an initial velocity as indicated in Fig. 26.

Fig. 27 shows the scaling of our World-Polyhedra algorithm with the number of surfaces in the world. We firstly see that there is a small computational penalty for doubling the number of faces. We also see linear scaling with an increase in world surfaces.

Fig. 28 shows the scaling of the World-Polyhedron algorithm with increased particle number. We see that again there is a small computational penalty for doubling the number of faces, which can be attributed to the SIMD of the GPU. The scaling with increasing particle number is once again linear.

Fig. 29 shows the scaling of the computational cost of Polyhedron–Polyhedron contact detection. We observe linear scaling with the number of particle faces and the number of particles.

### 5.3. Algorithm performance

Figs. 30–32 illustrate the large-scale performance of our algorithms for the simulation described in Fig. 27. We firstly analyze Polyhedron–Polyhedron collision detection, which is computationally the most expensive, in Fig. 31. We see that the trend of linear scaling holds up to 34 million particles, which is only limited by the current NVIDIA NVCC compiler.

The trend of linear scaling continues with the World-Polyhedron algorithm. However, it is significantly faster and takes 0.25 s for 34 million particles.

The broad-phase search algorithm [16] takes under one second a step for 34 million particles, with linear scaling as well, indicated in Fig. 32. Our results set a new performance level in contact detection for polyhedra in DEM.

Table 3 shows the comparison of our code to that of other authors using the Cundall Number  $C = N \times FPS$ , where a higher number represents better performance. Here FPS is the number of frames/steps that can be performed per second. Note: to the best of the authors knowledge there are no other GPU codes using polyhedral particles. Our code BLAZE-DEM (polyhedra) performs better than the others which use a non-spherical particle representation, while being able to simulate 136 times more particles than the fastest GPU code (Longmore et al.) in Table 3. Although the code by Radake et al. [6] performs the best it uses only spherical particles. Most of the algorithms presented in this paper is the same for spheres and our code BLAZE-DEM [16] using spherical particles is about 3 times faster as indicated in Table 3.

Fig. 33 shows the frequency of the two collision types depicted in Fig. 6. We see that indeed vertex–face is the dominant contact type and justifies our choice in searching for it first. In Fig. 33(a) we see that edge–edge contact is at most 10%. We note a similar trend in Fig. 33(b) where a slightly higher percentage of edge–edge contact can be attributed to the geometrical effect of the drum. In Fig. 33(c) edge–edge contact increases to 30% as the initial velocity of particles causes an impact with the drum resulting in a more random orientation. As the particles reach a macroscopic steady state, the edge–edge contact frequency decreases to be similar to the other simulations.

## 6. Conclusion

In this paper we have presented a novel approach for collision detection that is optimized for the GPU architecture. We evaluated the scaling of our algorithm and found favorable results in that the time does not necessarily scale with increased geometrical complexity for the system we have analyzed. We achieve a new performance level in DEM by simulating 34 million polyhedra (13 s per time step) on a single NVIDIA K6000 GPU.

## Acknowledgments

We gratefully acknowledge the support of NVIDIA Corporation with the donation of the GPU used for this research. This work was supported in part by CSIR SRP TA-2011-001.

## References

- [1] P. Cundall, O.D.L. Strack, A discrete numerical model for granular assemblies, *Geotechnique* 29 (1979) 47–65.
- [2] P. Cleary, The filling of dragline buckets, *Math. Eng. Ind.* 29 (1998) 1–24.
- [3] B. Mishra, R. Rajamani, Simulation of charge motion in ball mills. part 1: experimental verifications, *Int. J. Miner. Process.* 40 (1994) 171–186.
- [4] W. Ketterhagen, J. Curtis, C. Wassgren, Predicting the flow mode from hoppers using the discrete element method, *Powder Technol.* 195 (2009) 1–10.
- [5] M. Moakher, T. Shinbrot, F. Muzzio, Experimentally validated computations of flow, mixing and segregation of non-cohesive grains in 3d tumbling blenders, *Powder Technol.* 109 (2000) 58–71.
- [6] C. Radeke, B. Glasser, J. Khinast, Large-scale powder mixer simulations using massively parallel GPU architectures, *Chem. Eng. Sci.* 65 (2010) 6435–6442.
- [7] J. Latham, A. Munjiza, The modelling of particle systems with real shapes, *Philos. Trans. R. Soc. Lond. Ser. A: Math. Phys. Eng. Sci.* 362 (2004) 1953–1972.
- [8] P. Cleary, M. Sawley, Dem modelling of industrial granular flows: 3d case studies and the effect of particle shape on hopper discharge, *Appl. Math. Modell.* 26 (2002) 89–111.
- [9] D. Zhao, E. Nezami, Y. Hashash, J. Ghaboussi, Three-dimensional discrete element simulation for granular materials, *Comput. Aided Eng. Comput.: Int. J. Eng. Softw.* 23 (2006) 749–770.
- [10] D. Markauska, Investigation of adequacy of multi-sphere approximation of elliptical particles for dem simulations, *Granular Matter* 12 (2010) 107–123.
- [11] S. Mack, P. Langston, C. Webb, T. York, Experimental validation of polyhedral discrete element model, *Powder Technol.* 214 (2011) 431–442.
- [12] NVIDIA, Cuda 6, May 2014. <<http://www.nvidia.com/cuda>>
- [13] NVIDIA, Nvidia kepler gk110 architecture whitepaper, 2012. <<http://www.nvidia.com/NVIDIA>> KEPLER GK110 Architecture Whitepaper
- [14] J. Sanders, E. Kandrot, CUDA by example, vol. 12, 2010.
- [15] N. Bell, Y. Yu, Particle-based simulation of granular materials, *Eurographics/ACM SIGGRAPH Symp. Comput. Anim.* 25 (2005) 29–31.
- [16] N. Govender, D. Wilke, S. Kok, Development of a convex polyhedral discrete element simulation framework for NVIDIA kepler based GPUs, *J. Comput. Appl. Math.* 270 (2014) 386–400.
- [17] J.J. Jimenez, R.J. Segura, Collision detection between complex polyhedra, *Comput. Graphics* 32 (2008) 402–411.
- [18] B. Nassauer, T. Liedke, Polyhedral particles for the discrete element method, *Granular Matter* 15 (2013) 85–93.
- [19] C. Boon, G. Housby, S. Utili, A new algorithm for contact detection between convex polygonal and polyhedral particles in the discrete element method, *Comput. Geotech.* 44 (2012) 73–82.
- [20] B. Grunbaum, Convex Polytopes, 2nd ed., Volker Kaibel, ISBN 978-0-387-40409-7, 2003.
- [21] P. Langston, Distinct element modelling of non-spherical frictionless particle flow, *Chem. Eng. Sci.* 59 (2004) 425–435.
- [22] P. Cundall, Formulation of a three-dimensional distinct element model – part i: a scheme to detect and represent contacts in a system composed of many polyhedral blocks, *Int. J. Rock Mech.* 25 (1988) 107–116.
- [23] J. Longmore et al., Towards realistic and interactive sand simulation: a GPU-based framework, *Powder Technol.* 235 (2013) 983–1000.
- [24] E. Battey-Pratt, T. Racey, Geometric model for fundamental particles, *Int. J. Theor. Phys.* 19 (1980) 6.
- [25] T. Harada, GPU Gems 3: Real-time rigid body simulation on GPUs, vol. 3, 2008.
- [26] G. Neubauer, C.A. Radeke, GPU based particle simulation framework with fluid coupling ability (March 2014). <<http://on-demand.gputechconf.com/gtc/2014/poster/pdf/P4143>>.
- [27] N. Govender, D. Wilke, S. Kok, R. Els, A GPU based polyhedral particle dem transport code (March 2014). <<http://on-demand.gputechconf.com/gtc/2014/poster/pdf/P4126>>.